Numerical modeling of ocean-ice interactions under Pine Island Bay's ice shelf

Antony J. Payne,[1] Paul R. Holland,[2,3] Andrew P. Shepherd,[4] Ian C. Rutt,[1] Adrian Jenkins,[2] Ian Joughin[5]

Received 26 May 2007; revised 18 June 2007; accepted 2 August 2007; published 19 October 2007.

[1] A two-dimensional numerical model is used to simulate the dynamics of buoyant, meltwater-rich plumes flowing beneath the ice shelf occupying much of Pine Island Bay, West Antarctica. Recent studies have shown that this ice shelf, along with all others fringing the Amundsen Sea, is thinning rapidly. In the model, both the Coriolis effect and subshelf topography are important in controlling plume dynamics and the spatial distribution of ice melt. Melt is concentrated in a narrow zone within ~20 km of the grounding line where steep subshelf slopes and access to warm ambient water allow melt rates to exceed 100 m yr^{-1}. The plume generated by entrainment of ambient water into the meltwater in these areas is guided by the topography of the ice shelf underside and exits the ice shelf at three distinct outflow locations. Melt rates generated along the course of the plume are higher (approximately 2.5×) than rates elsewhere. The model suggests that the observed ice shelf thinning rates could have resulted from a hypothetical instantaneous 0.25°C warming of the ambient water entrained by the plume. A context for this value is provided by the 40-year warming trend documented by Jacobs et al. (2002) for Circumpolar Deep Water in the nearby Ross Sea.

Citation: Payne, A. J., P. R. Holland, A. P. Shepherd, I. C. Rutt, A. Jenkins, and I. Joughin (2007), Numerical modeling of ocean-ice interactions under Pine Island Bay's ice shelf, *J. Geophys. Res.*, *112*, C10019, doi:10.1029/2006JC003733.

1. Introduction

[2] A number of recent studies have established that contemporary (1990s onward) glaciological change in the West Antarctic ice sheet is centered along the coast of the Amundsen Sea. Satellite-based techniques including radar altimetry, synthetic aperture radar interferometry (SRI), and image feature tracking have identified thinning of the grounded [*Shepherd et al.*, 2002] and floating ice [*Shepherd et al.*, 2004] in the area, as well as the acceleration of the region's major ice stream (Pine Island Glacier, PIG) [*Rignot et al.*, 2002; *Joughin et al.*, 2003] and the retreat of this ice stream's grounding line [*Rignot*, 1998]. A consistent story has emerged that implicates changes in the oceanography of the Amundsen Sea as a possible triggering mechanism for these glaciological effects. It is hypothesized that these changes produce an increase in the rate of basal melt experienced by the area's floating ice shelves and, consequentially, the thinning of this ice. Such thinning then reduces the contact between partially floating ice near the grounding line (in the so-called ice plain [*Corr et al.*, 2001]) and the underlying bedrock, causing a reduction in basal drag and local acceleration [*Rignot*, 2002]. *Payne et al.* [2004] show that this acceleration can be transmitted over the entire upstream extent of PIG (some 200 km) on decadal timescales by a diffusive-type process.

[3] The aim of this study is to investigate possible links between the properties of the Amundsen Sea's water masses and the melt rates beneath its fringing ice shelves. We apply a newly created numerical model of a buoyant, meltwater-rich plume flowing across the ice shelf base and entraining the ambient waters of the Amundsen Sea. The geometry of our model domain and the oceanographic inputs are chosen to reflect conditions under the Pine Island Ice Shelf (PIIS), into which PIG flows. We employ the model in three ways. First, we assess the results of a standard model experiment in order to understand the controls on PIIS's melt and the dynamics of its buoyant plume. Second, we assess the sensitivity of results to the poorly constrained parameters within the model, such as those associated with the entrainment of the ambient water. Finally, we use the model to investigate the changes in the ambient water's temperature and salinity that would be required to produce the observed ice shelf thinning rates.

2. Model Description

[4] The model employed in this paper is described in detail by *Holland and Feltham* [2006], so we therefore limit

[1]Centre for Polar Observation and Modelling, University of Bristol, Bristol, UK.
[2]British Antarctic Survey, Cambridge, UK.
[3]Centre for Polar Observation and Modelling, University College London, London, UK.
[4]Centre for Polar Observation and Modelling, University of Cambridge, Cambridge, UK.
[5]Polar Science Centre, University of Washington, Seattle, Washington, USA.

0148-0227/07/2006JC003733

Table 1. Parameters Used in the Model

Symbol	Definition	Value[a]
c_L	constant in Kochergin entrainment relation	0.0275[b]
ρ_0	reference density	1030 kg m^{-3}
ρ_{fw}	density of freshwater	1000 kg m^{-3}
ρ_i	density of ice	910 kg m^{-3}
g	acceleration due to gravity	9.81 m s^{-2}
β_S	salinity coefficient in linear equation of state	7.86×10^{-4}
β_T	temperature coefficient in linear equation of state	3.87×10^{-5} °C^{-1}
S_0	reference salinity	34.5
T_0	reference temperature	−2.0°C
a	salinity constant in freezing point relation	−0.0573°C
b	constant in freezing point relation	0.0832°C
c	depth constant in freezing point relation	-7.61×10^{-4} °C m^{-1}
c_i	heat capacity of ice	2009 J kg^{-1} °C^{-1}
c_0	reference heat capacity of plume water	3974 J kg^{-1} °C^{-1}
L	latent heat of fusion of ice	3.35×10^5 J kg^{-1}
k_i	thermal conductivity of ice	2.1 W m^{-2} °C^{-1}
T_i	core temperature of ice shelf	−15.0°C[b]
K_h	horizontal eddy viscosity	100 m^2 s^{-1} [b]
f	Coriolis parameter	-1.415×10^5 s^{-1} (76° south)
c_d	dimensionless friction coefficient of shelf underside	0.003[b]

[a]Used in the standard experiment.
[b]Varied in the sensitivity analysis.

the present description to an outline of the key components of the model. The model is based on vertically integrated prognostic equations expressing the conservation of mass, momentum, heat, and salt for a plume flowing across the underside of a floating ice shelf and separating the ice from a passive ambient water mass below. The depth of the plume (D) extends between a lower surface separating the active plume from the ambient water mass (denoted by $z = A$, where z is height relative to sea level and positive upward) to its upper surface (denoted by $z = B$), which is either the ice shelf underside or the ocean surface. The model is unable to represent the separation of the plume from the ice shelf base, which would occur if the density of the plume approached that of the underlying ambient water. However, this does not occur to any significant extent in this study. The plume depth's temporal evolution (time t) over its two-dimensional horizontal extent (x, y) is governed by the rate of entrainment ($\dot{e}$) of the ambient water and the rate of melting and/or freezing ($\dot{m}$, positive for melting expressed in ocean water equivalents) of the overlying ice shelf, as well as the divergence of water flow within the plume:

$$\frac{\partial D}{\partial t} + \nabla \cdot (\mathbf{u}D) = \dot{e} + \dot{m}, \tag{1}$$

where $\mathbf{u}$ is the horizontal depth-averaged velocity field with u, v components in the x and y dimensions, respectively. We follow *Jungclaus and Backhaus* [1994] in employing the *Kochergin* [1987] parameterization of entrainment:

$$\dot{e} = \frac{c_L^2}{S_m}\sqrt{u^2 + v^2 + \frac{g'D}{S_m}}, \tag{2}$$

where c_L is a constant (see Table 1 for all parameter values), S_m is the turbulent Schmidt number, and g' is the reduced gravity, defined as

$$g' = g\frac{(\rho_a - \rho)}{\rho_o}, \tag{3}$$

where ρ is the density of plume water, ρ_a is the density of the ambient water (ambient properties are denoted using a subscript a throughout), and ρ_0 is a reference density for seawater. We use the formulation of *Mellor and Durbin* [1975] for the turbulent Schmidt number, which is itself a function of the Richardson number ($Ri = g'D/(u^2 + v^2)$):

$$S_m = \frac{Ri}{0.0725\left(Ri + 0.186 - \sqrt{Ri^2 - 0.316Ri + 0.0346}\right)}. \tag{4}$$

For values of the Richardson number above ~0.004 the Schmidt number is a quasi-linear function of the Richardson number, and the rate of entrainment is therefore proportional to the plume's velocity and inversely proportional to its Richardson number.

[5] The density of the ambient water has a depth-dependent distribution discussed in section 3, while the density of the plume is determined from its temperature (T) and salinity (S) using the linearized equation of state [*Jenkins and Bombosch*, 1995]:

$$\rho = [1 + \beta_S(S - S_0) - \beta_T(T - T_0)]\rho_0, \tag{5}$$

where the various empirical constants are again given in Table 1. The distributions of temperature and salinity within the plume are both assumed to be locally uniform across the plume's depth.

[6] The rate of melting or freezing is determined by solving equations representing the continuity of heat and salt fluxes across the ice/plume interface and the relationship of the freezing point with pressure and salinity [*Jenkins and Bombosch*, 1995]:

$$\dot{m}S_b = \gamma_S|\mathbf{u}|(S - S_b) \tag{6a}$$

$$\dot{m}L + \dot{m}c_i(T_b - T_i) = c_0\gamma_T|\mathbf{u}|(T - T_b) \tag{6b}$$

$$T_b = aS_b + b + cB \tag{6c}$$

where L is the latent heat of fusion of ice, c_i is the heat capacity of ice, ρ_i is the density of ice, and c_0 is the reference heat capacity of plume water. Equations (6a)–(6c) are solved simultaneously to yield a melt rate and the temperature and salinity at the interface (T_b and S_b, respectively; properties at the ice interface are denoted using a subscript b throughout). In equations (6a)–(6c), the turbulent diffusion coefficients for temperature and salinity (γ_T and γ_S, respectively) in the thin boundary layer separating plume and ice are determined using standard relations, which are dependent on the Reynolds number of the plume [*Holland and Feltham*, 2006; *Nicholls and Jenkins*, 1993]. In equation (6b), the second term on the left-

hand side approximates the heat conducted into the ice shelf as that required to warm the ice from the ice shelf core temperature (T_i) to the freezing point (T_b) [see *Holland and Jenkins*, 1999, equations (6), (26), and (31)].

[7] The momentum balance of the plume is expressed in depth-integrated form

$$\begin{aligned}\frac{\partial Du}{\partial t}+\nabla\cdot(D\mathbf{u}u)&=\nabla\cdot(K_hD\nabla u)+\frac{gD^2}{2\rho_0}\frac{\partial\rho}{\partial x}+g'D\frac{\partial A}{\partial x}\\&\quad-c_d|\mathbf{u}|u+Dfv\\\frac{\partial Dv}{\partial t}+\nabla\cdot(D\mathbf{u}v)&=\nabla\cdot(K_hD\nabla v)+\frac{gD^2}{2\rho_0}\frac{\partial\rho}{\partial y}+g'D\frac{\partial A}{\partial y}\\&\quad-c_d|\mathbf{u}|v-Dfu,\end{aligned}\tag{7}$$

where c_d is the friction coefficient for the underside of the ice shelf. The terms on the right-hand side represent horizontal turbulent mixing, the forcing associated with lateral differences in buoyancy within the plume, forcing associated with the density difference between plume and ambient water (proportional to the slope in the interface), the turbulent drag exerted by the ice shelf base, and Coriolis forcing.

[8] The vertically integrated heat and salt budgets yield prognostic equations for the depth-averaged temperature and salinity in the plume:

$$\begin{aligned}\frac{\partial DT}{\partial t}+\nabla\cdot(D\mathbf{u}T)&=\nabla\cdot(K_hD\nabla T)+\dot{e}T_a+\dot{m}T_b-\gamma_T|\mathbf{u}|(T-T_b)\\\frac{\partial DS}{\partial t}+\nabla\cdot(D\mathbf{u}S)&=\nabla\cdot(K_hD\nabla S)+\dot{e}S_a,\end{aligned}\tag{8}$$

where T_a and S_a are temperature and salinity, respectively, at the ambient/plume interface. Note that we assume the same values for eddy diffusivity and eddy viscosity in equations (7) and (8). The right-hand side of each equation contains sources and sinks of heat and salt, including entrainment from the ambient water, the effect of melting/freezing in terms of mass addition/loss to the plume, and the heat/salt diffused across the boundary layer to the ice shelf (for salinity the latter two terms cancel by equations 6a and 6b).

[9] There is a growing literature on the application of three-dimensional ocean models to the circulation within ice shelf cavities, and notable examples include the works by *Gerdes et al.* [1999], *Williams et al.* [2001], *Holland et al.* [2003], and *Jenkins et al.* [2004]. In this study we have opted to use the simpler approach of a vertically integrated, reduced gravity, plume model. The chief advantage of this approach is the short integration time, which allows us to explore model sensitivity to a range of parameters. The main disadvantage is that we must specify the ambient water properties throughout the cavity, and since we have no data to guide us, we can do little more than specify properties observed at the ice front everywhere. A further drawback with the reduced gravity approach is that we cannot assess the impact of any depth-independent flows within the cavity. Some, but not all, of the three-dimensional models mentioned above have indicated that the depth-independent flow is dominant within the cavities beneath the larger Antarctic ice shelves. However, those larger cavities are filled with ambient water near the surface freezing point, and the melt rates at the base of the ice shelves are thus 2 orders of magnitude lower than the ones we simulate here. The higher melt rates beneath PIIS imply stronger stratification of the water column and imply a reduced role for the depth-independent flow. We therefore argue that the plume model provides a satisfactory simulation of the behavior of the buoyant upper layer of water that interacts with the ice shelf base, and we show in section 5 that the simulated plume paths agree well with the limited evidence available. Nonetheless, it is important to note that the omitted three-dimensional circulation effects will have important implications for the flow of denser water into the cavity and hence for the (specified) properties of the ambient water entrained into the plume (see section 3).

3. Model Forcing, Boundary, and Initial Conditions

[10] The model requires four basic types of input: information on the properties of the ambient water mass; the geometry of the ice shelf's lower surface, across which the plume will flow; boundary conditions at the grounding line and in the open ocean; and initial conditions. The best available oceanographic data with which to drive the model are measured profiles of temperature and salinity close to the ice shelf front from a hydrographic survey in March 1994 [*Jacobs et al.*, 1996]. The locations of the three survey stations, which extend continuously from the ocean surface to the seabed, are shown in Figure 1. Note that in assuming that these observations are a valid means of estimating the properties of the entrained ambient water throughout the subshelf cavity, we are implicitly assuming that the ambient water mass is at rest or flowing very slowly. This assumption is supported by the very close similarity between the three profiles despite their varied locations across the embayment. We approximate these observations using the following piecewise-linear functions:

$$\begin{aligned}T_a&=\begin{cases}-1.9-4.67\times10^{-3}B & 0\text{ m}>B>-600\text{ m}\\1.0 & B\le-600\text{ m}\end{cases}\\S_a&=\begin{cases}33.8-1.50\times10^{-3}B & 0\text{ m}>B>-600\text{ m}\\34.7 & B\le-600\text{ m.}\end{cases}\end{aligned}\tag{9}$$

[11] We constructed a digital elevation model of the underside of the ice shelf using data from a gridded data set of ice surface elevation [*Bamber and Bindschadler*, 1997]. The template of the ice shelf was extracted using the grounding lines mapped by *Rignot* [1998] around the mouth of PIG and information from the Antarctic Digital Database (ADD) grounding line data set elsewhere and using the 1996 ice front position of *Schmeltz et al.* [2002]. Information on the elevation of the upper surface of a freely floating ice shelf (s) can readily be used to determine the elevation of the lower surface if the vertically averaged density of the ice shelf ($\tilde{\rho}_i$) is known (which is assumed to vary spatially and will be somewhat lower than ρ_i because of accumulated snow) and a constant ocean density is assumed:

$$(s-B)\times\tilde{\rho}_i(x,y)=-\rho_0B.\tag{10}$$

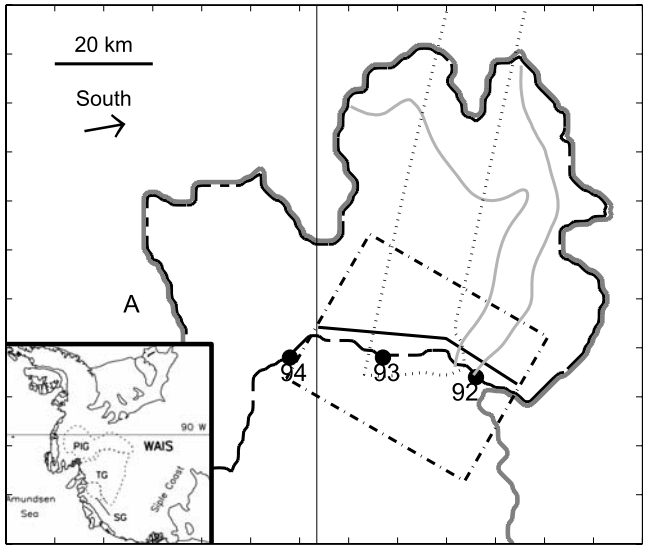

Figure 1. Ice shelf geometry used in the model experiments with inset showing PIIS's location (shaded grey) relative to the catchment areas of PIG, Thwaites Glacier (TG), and Smith Glacier (SG). The heavy grey line indicates the grounding line position, while the thinner black line delimits the ice shelf domain. Black dots indicate the location of the three hydrographic stations reported by *Jacobs et al.* [1996] with associated station numbers. The black vertical line separates what we refer to as PIIS proper (to the right) from an area of stagnant ice shelf to the left. The label A is referred to in the text, while the dotted line shows the flight line reported by *Corr et al.* [2001]. The two light grey curves show the locations of the streamlines shown in Figure 8; the dash-dotted box shows the location of the ASTER image in Figure 11; and the heavy black line shows the location of the transect shown in Figure 12. The model domain is centered at 75°S, 101°W, approximately.

[12] We derived an empirical relationship between ice thickness and freeboard using the sparse airborne data of *Corr et al.* [2001] and the gridded data of *Bamber and Bindschadler* [1997], respectively. This relationship implies that $\tilde{\rho}_i$ varies between 885 and 901 kg m^{-3} along the *Corr et al.* [2001] flight lines. We then applied this model to predict thickness over the entire ice shelf from the gridded ice surface elevation data.

[13] Initial testing of the model with these data predicted anomalously high melt rates which arise because of very deep, steeply sloping ice in the area labeled A in Figure 1. We believe that this feature of the data set is incorrect for two reasons. First, it implies water depths of over 1 km, while the only available bathymetric information for the area [*Jacobs et al.*, 1996; *Lowe and Anderson*, 2002] suggests that the 1-km-deep trough which underlies the main part of PIIS does not extend into this area and that water depths shallow to between 400 and 500 m. Second, the flow of the ice shelf in this area is virtually stagnant [*Joughin et al.*, 2003; *Rignot et al.*, 2002], while the steep surface slopes of the data set suggest that rapid ice flow should prevail. We therefore believe that the ADD grounding line position in this area is incorrect and have advanced it by 8 km. The resulting final elevation model of the underside of the ice shelf is shown in Figure 2. We note that it is consistent with the flight lines reported by *Corr et al.* [2001] in the vicinity of PIG.

[14] In order to solve equations (1)–(8), boundary conditions are required at the edges of the numerical domain. In the present application these correspond to the ice sheet grounding line and the ice shelf front. The thickness of the plume near the grounding line, its temperature, and its salinity are assigned to an "inflow" mixed layer, and the velocity is then calculated according to this water's buoyancy. We set the plume thickness to 1 cm for the ~40-km-wide grounding line of PIG [see *Rignot*, 1998] and assume zero plume thickness for the segments of the grounding line outside of this area. The temperature and salinity of the inflow mixed layer at the PIG grounding line were set using the theory of *Gade* [1979]; we cool and freshen the ambient water at the depth of the inflow in a manner consistent with the release of meteoric ice meltwater into the ambient seawater until the resulting water mass is almost at the freezing point.

[15] The boundary with the open ocean is slightly more complicated because the appropriate boundary conditions are of Neumann type; in particular, we assume zero gradients. The highly irregular geometry of the ice front makes the application of this type of boundary condition at the front itself rather unwieldy. We therefore extend our model domain to incorporate some areas of open ocean to the west of the ice shelf (see Figure 2) and apply our boundary conditions at the orthogonal edges of the extended domain. Unfortunately, this approach introduces into the model domain some very steep topographic gradients at the ice shelf front, which lead to problems of numerical stability. These issues were solved by introducing an artificial thickness of ice over the open ocean, which formed a ramp

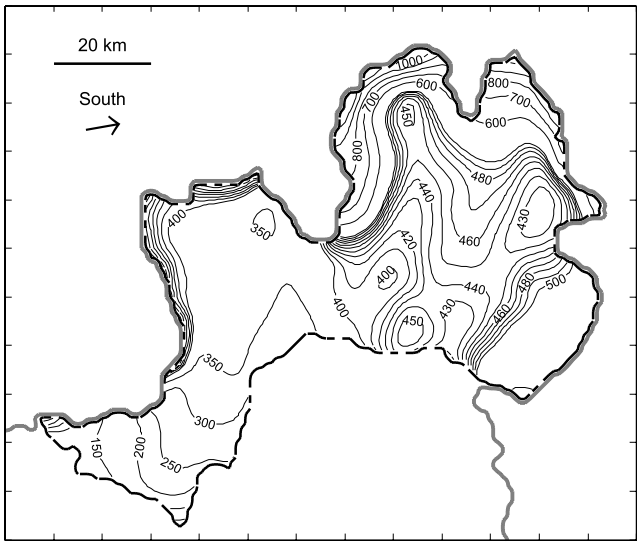

Figure 2. Ice shelf geometry used in the model experiments. Contours refer to the depth below sea level of the underside of the ice shelf (in m) and are based on 1-km-resolution digital elevation model. The contour interval between 400 and 500 m is 20 m; 50 m below 400 m; and 100 m above 500 m.

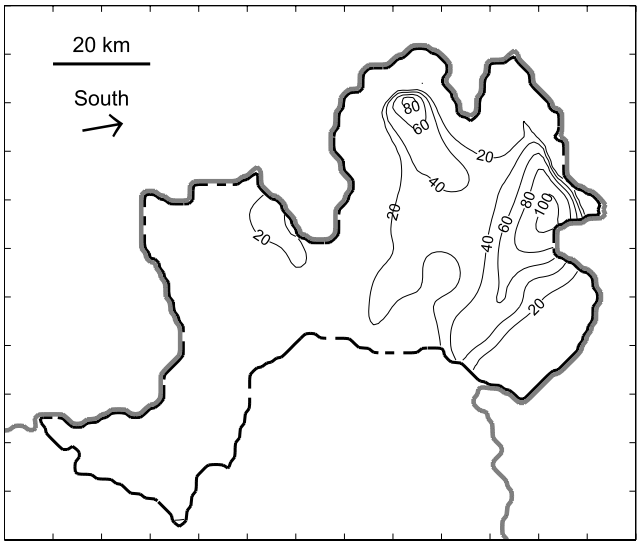

Figure 3. Simulated mean plume thickness (m) for final 10 days of the standard 20-day experiment.

between the ice shelf front and the western domain boundary. We believe that this construct does not affect model predictions under the ice shelf because plume flow is always outward from the shelf to the ocean and in our experiments the open ocean plume is always thinner than that under the ice shelf proper. Although the possibility of gravity waves moving in the opposite direction to plume flow (i.e., from open ocean to shelf) exists, we see no obvious signs of them in our results. Only results from beneath the ice shelf proper will be presented in this paper. In this study we assume that the plume is present everywhere as a "mixed layer." Therefore initial conditions for plume thickness, temperature, and salinity are required throughout the domain. We selected a value of 1.0 m for thickness and set temperature and salinity to their ambient values at the appropriate water depths. The results of the model after a typical 20-day integration show no dependency on these values.

4. Numerical Implementation and Standard Experiment

[16] The equations outlined in section 2 were solved using standard finite difference techniques on a regular 1-km grid using a fixed time step of 60 s. The numerical implementation follows the work of *Jungclaus and Backhaus* [1994] using a staggered Arakawa C grid [*Mesinger and Arakawa*, 1976] for the spatial discretization and explicit two-level stepping in time. Although the numerical scheme incorporates the ability to cope with a time-dependent plume extent (using the wetting/drying scheme of *Jungclaus and Backhaus* [1994]), this facility was not required in the present experiments because the whole of the ice shelf and open ocean domains experience plume flow. Similarly, the ability of the numerical implementation to simulate frazil ice formation [*Holland and Feltham*, 2006] was not required in the generally warm water experiments reported here. All experiments were run for a simulated period of 20 days, although less than 10 days was generally required for equilibrium to be established. However, even after 20 days, the plume showed some small-scale cyclic variability in the high-slope regions close to PIG's grounding line. For this reason, we present only results averaged over the final 10 days of each simulation (the mean of 11 daily data sets), unless otherwise noted. The reason for the variability is uncertain and may be partially numerical in nature.

[17] The "standard" experiment reported below employs parameter values selected as the result of a manual tuning exercise employing the constant in the Kochergin entrainment relation (c_L), the core temperature of ice shelf (T_i), the horizontal eddy viscosity (K_h), and the dimensionless friction coefficient of the ice shelf underside (c_d). The tuning target was the mean melt rate over the whole ice shelf as determined from the ice divergence calculations discussed in section 4. Subsequently, a sensitivity analysis was performed for each parameter in turn; this is reported in section 5. The standard values for each parameter are

$$c_L = 0.0275$$
$$T_i = -15^{\circ}\mathrm{C}$$
$$K_h = 100\ \mathrm{m^2\ s^{-1}}$$
$$c_d = 0.003.$$

[18] The values for the friction coefficient and the Kochergin-entrainment parameter are those employed by *Jungclaus et al.* [1995] in their two-dimensional, horizontal plane study of density currents in the Fram Strait. Both are also typical of values used for sub–ice shelf simulations (e.g., *Jenkins* [1991] uses c_d = 0.0025 and *Holland and Feltham* [2006] use c_l = 0.0245). The value for eddy diffusivity in the horizontal compares to values of 400 $\mathrm{m^2\ s^{-1}}$ used by *Hellmer et al.* [1998] in a two-dimensional vertical plane experiment and 100 $\mathrm{m^2\ s^{-1}}$ employed by *Grosfeld et al.* [1997] and *Gerdes et al.* [1999] in three-dimensional simulations. A potential range for the core ice temperature is delimited by the expected temperature at the base of the

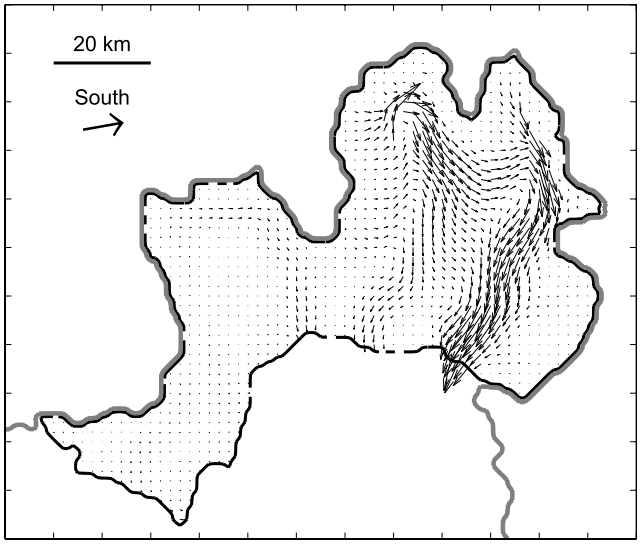

Figure 4. Simulated mean flux field over final 10 days of the standard experiment. Length of arrows is scaled linearly to a maximum flux magnitude of 60 $\mathrm{m^2\ s^{-1}}$ with flux at every second model grid point shown to improve clarity.

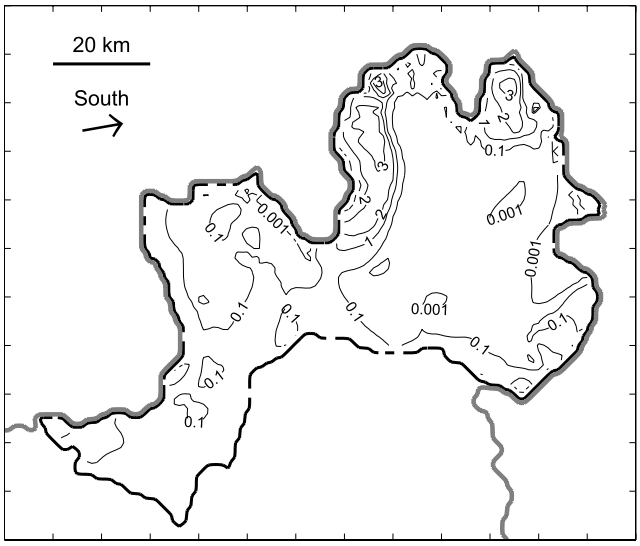

Figure 5. Simulated mean rates of entrainment from the underlying ambient water mass ($\times 10^{-4}$ m s^{-1}) over final 10 days of the standard experiment.

grounded ice (the pressure-dependent melting point ~ -2°C) and estimated mean annual air temperature at the ice surface. The latter varies between -23°C on the ice shelf and -28°C at the ice divide which is drained by PIG [*Giovinetto et al.*, 1990]. Horizontal advection within PIG is likely to ensure that middepth temperatures within it, and the ice shelf will approach -28°C. Our core ice temperature of -15°C is therefore warmer (by approximately 10°C) than glaciological observations would suggest. However, *Jenkins* [1999] estimates an ice temperature of -15°C from the temperature and salinity data of the March 1994 hydrographic survey, so that this temperature is consistent with oceanographic observations (note, however, that *Hellmer et al.* [1998] estimate -20°C from the same data). We return to this topic in section 5.

[19] Results from the tuned standard experiment for equilibrium plume thickness, horizontal fluxes of plume water, and rates of entrainment and melt are shown in Figures 3, 4, 5, and 6, respectively. It is important to stress that the definition of our standard experiment is fairly arbitrary and the tuning target was chosen to facilitate the comparisons made in section 5. The sensitivity of the model to the Kochergin entrainment coefficient (see section 6) means that the model could easily be tuned to any realistic value of mean melt rate (including those already in the literature and discussed in section 5). However, it should be noted that with the exception of core ice temperature, all of the parameter values lie very close to a priori expectation.

[20] The plume that develops within our model is fed primarily by entrainment in a 15-km-wide zone close to the grounding line of PIG and extending $\sim$40 km seaward (Figure 5). In this zone, rates of entrainment often exceed 0.2 mm s^{-1}; however, these rates rapidly fall by at least an order of magnitude to values <0.01 mm s^{-1} over the rest of the ice shelf. The path of the plume across the ice shelf underside is controlled by a combination of the Coriolis effect and ice shelf topography (Figure 4). The two principal outflows follow inverted channels in the ice shelf underside on either side of PIIS proper (i.e., in the area to the right of the vertical line shown in Figure 1). The path that water takes to these channels lies along lines of equal ice shelf draft and the flow of the plume is therefore likely to be close to geostrophic. A far smaller outflow to the north carries plume water generated in the stagnant portion of the ice shelf. Variations in plume depth (Figure 3) largely reflect ponding within enclosed channels in the ice shelf underside topography (see Figure 2). Outside of these areas, the plume has a typical depth of $\sim$20 m, and its interface with the ambient water (the sum of plume depth and ice shelf bathymetry, not shown) takes the form of an inclined plane in the areas of outflow, which again suggests that a geostrophic balance is operating.

[21] The model generates a total flux of plume water of 0.16 Sv (over the whole 4780 km^2 domain, or 0.13 Sv over the 3010 km^2 of PIIS proper) of which only $\sim$2% is meltwater, the remainder being entrained ambient water. The flow of water from the inflow mixed layer at the grounding line (0.25 km^3 yr^{-1} or 8×10^{-6} Sv) is an insignificant part of the outflow.

[22] The spatial distribution of melt predicted by the model is shown in Figure 6 and reflects two main patterns. The primary pattern is of high melt rates close to (but not at) the grounding lines associated with PIG and in the area extending $\sim$40 km farther seaward. In this area, melt rates are predicted to exceed 100 m yr^{-1}. The second feature of this pattern is that intermediate melt rates of $\sim$25 m yr^{-1} are associated with the path of the plume as it flows toward the ice shelf front (see Figure 4). Outside of these areas, melt rates are relatively low (<10 m yr^{-1}). The distribution of plume temperature above the local melting point ($T - T_b$) is shown in Figure 7 and is indicative of the amount of energy locally available in the plume to support melting. The areas of very high melt rate are associated with plume water that is $\sim$2°C above the interface freezing temperature, where the ambient water has a temperature of $\sim$1°C and the interface

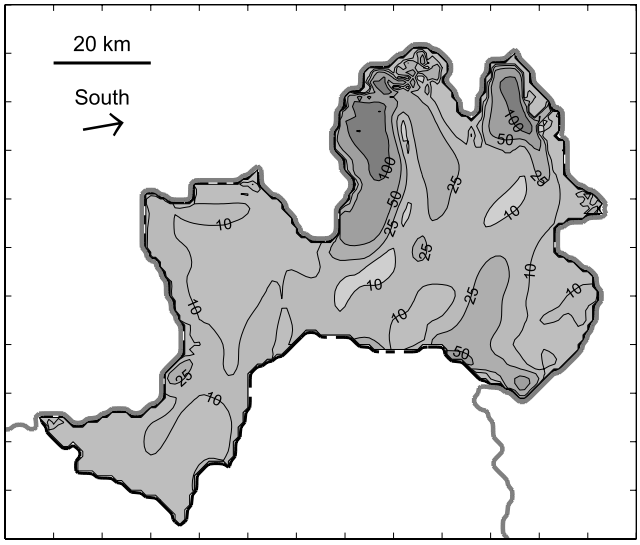

Figure 6. Simulated mean rates of melting from the overlying ice shelf (m yr^{-1}) over final 10 days of the standard experiment. The maximum rate in this field is 150 m yr^{-1}.

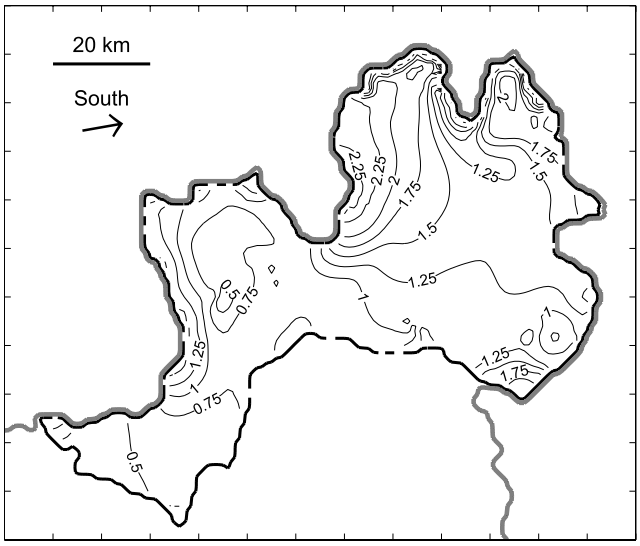

Figure 7. Temperature of the plume relative to local melting point (°C) as calculated using equation (6c).

pressure melting point is ~−1°C (at ~1000 m depth). This temperature is higher than the seawater freezing temperature because the rapid melting gives rise to considerable freshening. The remainder of the plume is characterized by a temperature of ~1.25°C above the interface freezing temperature but experiences an order of magnitude less melt. The reasons for this nonlinear response will now be discussed.

[23] Figure 8 shows the distribution of heat gained from entrainment (Q_e) and used in melting (Q_m) along the two streamlines identified in Figure 1 and calculated as

$$\begin{aligned} Q_e &= \rho_0 c_0 (T_a - T)\dot{e} \\ Q_m &= \rho_{fw} L\dot{m}. \end{aligned} \tag{11}$$

We will first analyze the predicted pattern of heat entrainment and then indicate how this affects the predicted pattern of melt. The Richardson number for these streamlines (and indeed for the whole model domain) almost always falls into the region (above 0.004) in which the Schmidt number (equation (4)) assumes a quasi-linear relation to the Richardson number, so that the rate of

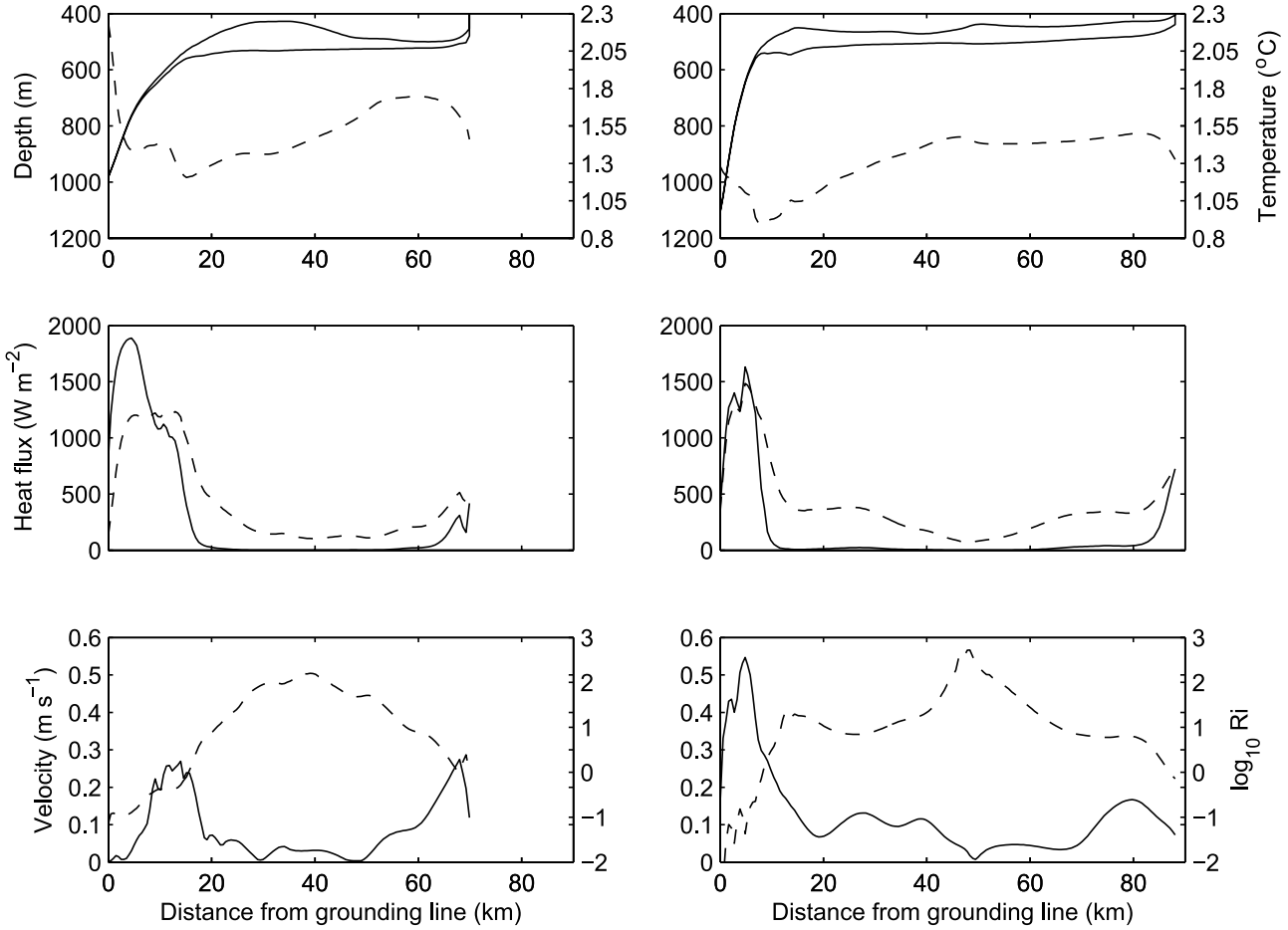

Figure 8. (right) Profiles of the position of the ice shelf base and plume-ambient interface (m, Figure 8 (top), solid line) with ambient temperature minus plume temperature (°C, Figure 8 (top), dashed line); heat fluxes associated with entrainment and melting (W m^{-2}, Figure 8 (middle), solid line entrainment and dashed line melting); and plume velocity (m s^{-1}) with Richardson number (Figure 8 (bottom), solid line velocity and dashed line log$_{10}$ of Richardson number) for the two streamlines identified in Figure 1. (left) More southerly streamline.

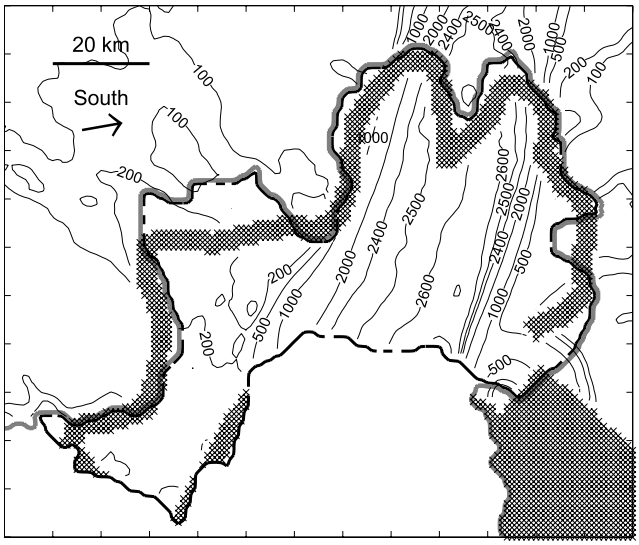

Figure 9. Magnitude of horizontal ice velocity (m yr^{-1}) as determined by satellite radar interferometry for 1992 and 1996 [*Joughin et al.*, 2003]. Cross-hatching indicates areas where no data were available due to lack coherence between radar images.

entrainment is proportional to the plume's velocity and inversely proportional to its Richardson number. Predicted Q_e rises sharply within the first 10 km of the grounding line where low Richardson numbers (implying less stable stratification) are prevalent. In the case of the northerly profile this effect is reinforced by high velocities near the grounding line, while in the southerly profile a plateau in Q_e at around 15 km is generated by a local velocity maximum. In both profiles, Q_e then falls as a function of both high Richardson number (stable stratification) and low velocity until the final 10 km of each streamline, which is characterized by increasing Q_e as velocities rise and Richardson number falls. In the model, areas of low Richardson number are primarily caused by low reduced gravity (equation (3)) as the density of the plume approaches that of the ambient water mass. Interestingly, the temperature difference between the plume and the ambient water is generally a poor predictor of Q_e, except close to the grounding line of the southerly profile.

[24] In both profiles the majority of heat gained by entrainment is used in melting within ~10 km, and the peaks of the two heat flux curves coincide closely. The integrals of Q_e and Q_m are in approximate balance over the southerly profile, while lateral convergence in the flow of the plume brings warm waters into the northerly profile and allows total Q_m to exceed total Q_e.

[25] The obvious link between entrainment and melting is that the former provides a heat source for the latter by raising the temperature of the plume. However, a second link is that both melt and entrainment rates are partially controlled by the velocity of the plume, which enters into equation (2) (both directly and via the Schmidt number, equation (4), so that there is a quasi-cubic dependence on velocity overall), while the thermal diffusion term (involving γ_T) in equations (6a)–(6c) is also a function of velocity [*Holland and Feltham*, 2006]. This second effect ensures that areas of high entrainment are also areas where melt can take advantage of the increased plume temperature, and it is responsible for the nonlinear relationship between plume temperatures and melt noted above because plume velocities over the majority of the ice shelf are very much lower than those near the grounding line (which limits the melt rates experienced in these areas).

5. Comparison to Available Observations and Previous Work

[26] Before entering into a comparison of the model's predictions with previous work and other available observations, we outline the process by which we obtained our estimate of the mean melt rate for the ice shelf and its spatial distribution. The equation of mass continuity for the ice shelf can be used to determine melt rates given information on ice shelf thickness, surface mass balance, and velocity:

$$\frac{\rho_0}{\tilde{\rho}_i}\dot{m} + \frac{\partial(s-B)}{\partial t} - M = -\nabla\cdot[\mathbf{u}_i(s-B)], \qquad (12)$$

where all terms are expressed in ice-equivalent units (with a multiplier to convert from our melt rate expressed in ocean water equivalents) and $\mathbf{u}_i$ is the horizontal ice velocity field and M is mass balance of the upper surface. Few data exist on the surface mass balance of the ice shelf but *Jenkins et al.* [1997] suggest a slight net loss of -0.4 m yr^{-1} (i.e., surface sublimation exceeds snow accumulation). The rate of ice thickness change (second term on the left-hand side of equation (12)) has been measured as -3.9 ± 0.5 m yr^{-1} between 1992 and 2001 (i.e., thinning) by *Shepherd et al.* [2004] using satellite radar altimetry; however, the horizontal resolution of the satellite data is too coarse to allow the spatial dependency of this term to be established with any accuracy. We assume that the *Jacobs et al.* [1996] data used to force the model is from a period during which this thinning was actively occurring (the surveys were actually conducted in 1994).

[27] The horizontal velocity of the ice shelf in 1992 and 1996 was determined using SRI by *Joughin et al.* [2003], and these data are shown in Figure 9. Uncertainties in tidal amplitude precluded a SRI velocity solution in a 5-km strip close to the grounding line. In order to construct a mean melt rate for the whole ice shelf we used linear interpolation (of each velocity component separately) to fill these data gaps. Close inspection of the velocity patterns upstream and downstream of PIG's grounding line suggests that this procedure is valid there; however, its validity elsewhere is uncertain. Ice thickness is easily found using equation (10) from our ice shelf bathymetry (Figure 2). The divergence calculation in equation (12) was performed on the 1-km grid, and the estimated melt rates are shown in Figure 10.

[28] The mean melt rate based this on ice flux divergence calculation is 18.4 m yr^{-1} overall and 26.2 m yr^{-1} in PIIS proper or 20.7 and 29.4 m yr^{-1} ice equivalent, respectively. These values are heavily influenced by estimated melt rates close to PIG's grounding line and may contain artifacts produced by the linear interpolation employed there. We

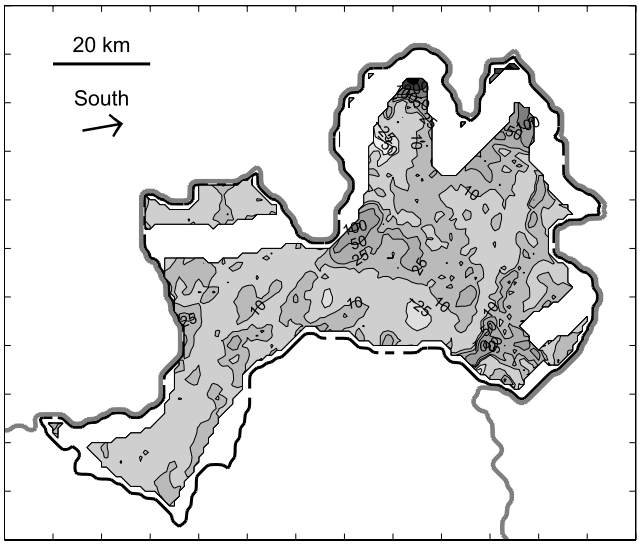

Figure 10. Melt rate (m yr^{-1}) determined from a flux divergence calculation for the ice shelf using ice thickness information derived from Figure 2 and the velocity information shown in Figure 9. The grey scale used is the same as in Figure 6 to facilitate comparison. The highest (darkest) two levels refer to melt rates of 200 and 300 m yr^{-1}. Areas for which no velocity data are available have been left blank.

therefore suspect that they may be overestimates. This could partially explain the suspiciously warm core ice temperatures required in the standard experiment, since these melt rates were used as tuning targets.

[29] Estimates of mean melt rate are also available from oceanographic and glaciological observations. These range from 10–15 m yr^{-1} [*Jacobs et al.*, 1996; *Jenkins et al.*, 1997; *Shepherd et al.*, 2004] up to a maximum of 24 ± 4 m yr^{-1} [*Rignot*, 1998]. The latter average was based on ice flux divergence calculations (hence likely units are ice equivalents) and included average values of 50 ± 10 m yr^{-1} for the first 20 km from the grounding line. Differences with the other satellite-based study [*Shepherd et al.*, 2004] are likely to reflect the different spatial-sampling methodologies employed; in the present paper we estimate melt rate for the whole ice shelf on a 1-km grid and then average this field, while *Shepherd et al.* [2004] obtain their equilibrium melt rate of 11 ± 1 m yr^{-1} by estimating thinning and ice flux divergence only at the specific points where altimetry crossing points were available. The latter approach results in sparse sampling regime with ~20 km between data points and is very likely to miss the highly localized melt peaks shown in the present study. The value of 12 ± 1 m yr^{-1}, obtained by *Jenkins et al.* [1997], was based on the difference in ice flux measured at two cross-stream thickness profiles. The upstream one of these now appears to have been too far downstream to sample the thickest floating ice on the southern side of the ice shelf, leading to an underestimate of the inflow to the ice shelf and hence an underestimate of the overall mass loss by melting.

[30] The comparison with the oceanographic estimates is worthy of further comment. *Jacobs et al.* [1996] cite a total flux of 0.172 Sv and a shelf area of 3×10^3 km^2, which are both similar to our estimates mentioned above. *Jacobs et al.* [1996] then use a net freshening of 0.183 with inflow salinity of 34.7 to obtain their melt estimate (believed to be in ice equivalents). A freshening of 0.5 would be needed to yield a melt rate similar to ours. On the basis of *Jacobs et al.*'s [1996] data, this strength of freshening is possible if one estimates the average outflow salinity from observed salinities between 100 and 600 m depth rather than the 340 to 800 m depth range that they employ (based on the assumption that meltwater could only appear below the draft of the ice shelf). This would require either that the plume water rises very rapidly between crossing the ice shelf front and reaching the survey station (within ~500 m of the front [*Jenkins et al.*, 1997]) or that there is intense vertical mixing at the shelf front.

[31] The only previous published modeling study of ice-ocean interaction under PIIS [*Hellmer et al.*, 1998] determined a mean melt rate of 12.5 m yr^{-1} with peak values of ~20–30 m yr^{-1} in experiments that were analogous to those described here. However, the model of *Hellmer et al.* [1998] considered a vertical slice through the sub-ice cavity and the grid resolution necessitated some smoothing of the subshelf topography. Results showed a strong sensitivity to the unknown bedrock topography, which controlled how far into the cavity the warmest waters could penetrate. A reasonable choice of bedrock shape was made, but this effectively tuned the model to match the best estimates of the mean melt rate that were available at the time [*Jacobs et al.*, 1996; *Jenkins et al.*, 1997]. These estimates now appear to be low.

[32] We now compare the spatial patterns predicted by the model with three different types of information: estimates of basal melt rates based on the ice flux divergence calculation, the location of polynyas at PIIS's ice front, and the composition of the plume water recorded by *Jacobs et al.* [1996].

[33] The spatial mean melt rate has been discussed previously and was used as a tuning target; however, the spatial pattern around this mean was not tuned in the model (indeed, it is a very robust feature of the model, see section 4). The patterns shown in Figures 6 and 10 (model prediction and ice flux estimate) have a number of points of similarity, as well as some differences. Both distributions have peak melt rates in excess of 100 m yr^{-1} near the grounding line of PIG and to the west in the same embayment; however, the exact locations of these peaks differ. Both distributions also have secondary peaks near the southwest sector of the ice front (following the predicted path of the plume) and are typified by relatively low melt rates of ~10 m yr^{-1} elsewhere. The major points of disagreement are the patches of freezing >50 m yr^{-1} near the PIG's grounding line. We believe that these are physically unrealistic artifacts that are most likely to be due to inaccuracies in our thickness data. We note that melt rates of ~100 m yr^{-1} within 10 km of the grounding line are consistent with the flight lines discussed by *Corr et al.* [2001] if one assumes that the downstream thinning that they observe is due entirely to mass loss and not tensile strain (this contention is supported by Figure 9). An ice velocity of ~2.5 km yr^{-1} suggests a 4-year transit time for ice in this zone, in which time, 300 to 500 m of

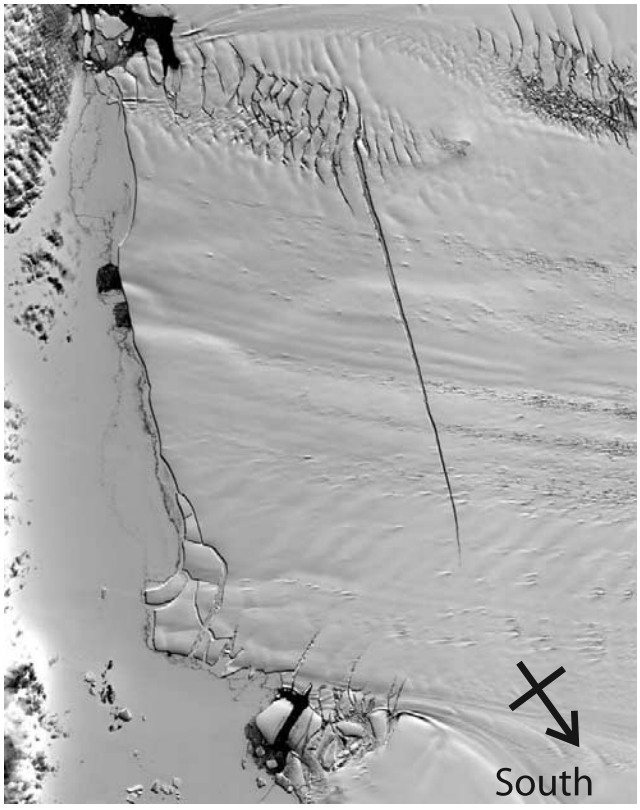

Figure 11. Imagery from the ASTER satellite shows detail of the PIIS ice front during December 2000. This section of the ice front approximately coincides with the ice front transect shown in Figures 1 and 12. The actual ice front in our topographic data (and shown in Figure 1) is in a position some 10 km landward of the front shown here. The ice shelf is to the right in the image with a large crevasse running vertically, while fast sea ice is to the left. The image shows approximately 50 km of ice front, which is characterized by many kilometer-sized icebergs.

ice is lost from the two 1998 flight lines at an average of 75 to 125 m yr^{-1}.

[34] Evidence for the spatial distribution of the predicted plume is difficult to obtain; however, Figure 11 shows the location of three reasonably persistent polynyas close to PIIS's ice front. The fast sea ice in this Advanced Spaceborne Thermal Emission and Reflection Radiometer (ASTER) image appears to have retreated from the ice shelf in three isolated locations, which correspond to the locations of the three main outflows predicted by the model (Figure 4). We therefore suggest that the sea ice in these areas is experiencing enhanced melt due to upwelling of the warmer plume water. This interpretation suggests that the topographic control exhibited by the modeled plume is reasonably accurate.

[35] Finally, the predicted composition of the modeled plume as it crosses the ice shelf front in its southwest sector can be compared to the temperature and salinity profiles at [*Jacobs et al.*, 1996] station 92. These profiles are characterized by near-constant temperature and salinity below a depth of 800 m. *Jacobs et al.* [1996] believe this water to be derived from upper Circumpolar Deep Water (CDW). Above 800 m, both temperature and salinity decrease steadily to the ocean surface. The modeled outflow temperature of -1.1°C and salinity 33.9 (Figure 12) are close to the values recorded in the most concentrated part of the outflow between depths of 100 and 200 m at station 92. There is evidence of meltwater at depths down to 800 m at this station, suggesting that in reality the plume detaches locally from the underside of the ice shelf. These detached plumes are generally warmer than -1.1°C, implying that they have become detached at greater depths, closer to the grounding line.

6. Sensitivity Analysis

[36] We investigate the influence of parameter uncertainty on our results by conducting a set of experiments in which each of four poorly constrained parameters are individually varied in turn. The results of this analysis are summarized in Figure 13 for the friction coefficient, horizontal eddy viscosity, entrainment coefficient, and core ice shelf temperature. The ranges used in these experiments are based, where possible, on values used in previous modeling studies. We believe that these ranges are the widest likely in each case. In all cases the spatial melt pattern underlying the mean values shown in Figure 13 was very similar to that of the standard experiment. The slight variation in results between adjacent parameters is thought to be due to averaging of the time dependence noted in section 4.

[37] Model results for eddy viscosity, temperature, and entrainment coefficient all show a monotonic response of melt to changes in the parameter value. In the case of the entrainment coefficient, there is a suggestion that this increase slows to a plateau at $\times 1.5$ the standard value. This parameter also has by far the largest effect on predicted melt rates, which reflects the crucial role of entrainment in bringing the heat into the plume that is subsequently used in melting. Clearly, increasing the value of the Kochergin coefficient allows more water to become entrained, which represents a larger heat source. Changes in the value of this parameter are expected to have a large effect because its squared value is used in equation (2). The predicted reduction in melt with cooler ice shelf temperature is also self-explanatory. We interpret the effect of the remaining parameters in terms of changes to the controls on plume velocity (and hence entrainment and melt rates as discussed in section 5). We suggest that the decrease in melt with increasing eddy viscosity reflects the lateral loss of momentum from rapidly flowing water near the grounding line to more slowly flowing areas of the plume. This reduced velocity then slows melt rate via its effect on both entrainment and heat diffusion at the ice/plume interface. The response to changes in the friction coefficient is more complex and predicted mean melt rates peak at a friction coefficient of 0.004. The decline in melt above this value reflects the dependence of melt on plume velocity mentioned in section 4 (greater friction obviously implying slower velocity), while the rise toward the maximum is likely to be a function of the direct role of friction in determining the turbulent diffusion coefficients that partially control melt rates (equations 6a and 6b) [*Kader and Yaglom*, 1977]. *Holland and Feltham* [2006] find similar effects in

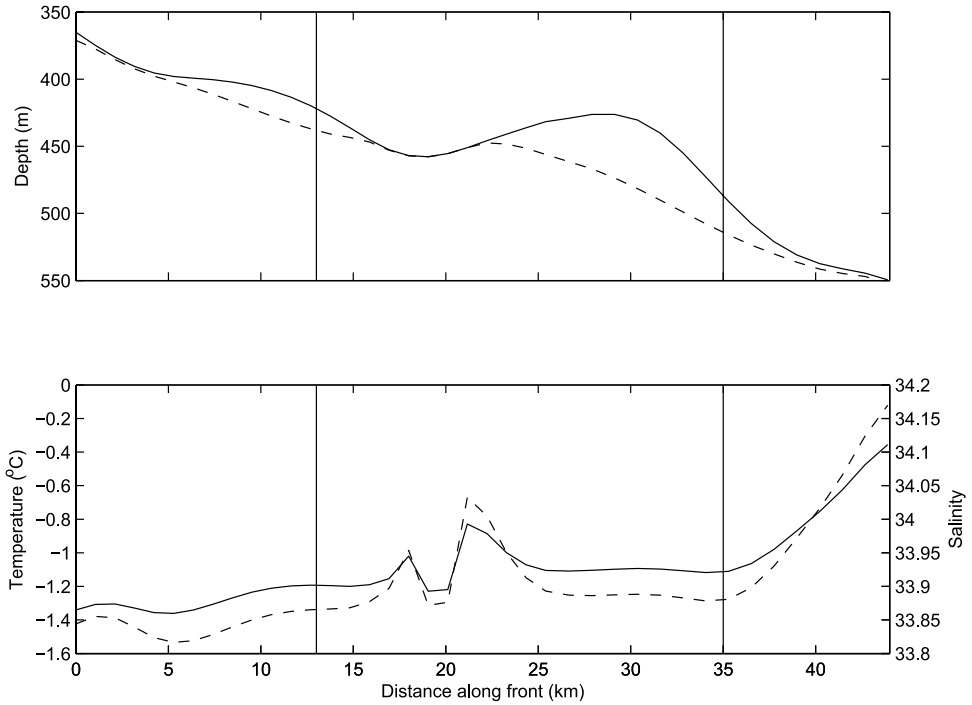

Figure 12. (top) Predicted plume geometry (solid line ice shelf base, dashed line plume/ambient interface) and (bottom) properties (solid line temperature, dashed line salinity) along a transect ~5 km behind the model's ice front (see Figure 1 for exact location). The vertical lines indicate the position of hydrographic stations (right) 92 and (left) 93 reported by *Jacobs et al.* [1996].

their sensitivity analysis of plume flow under an idealized ice shelf.

7. Perturbation of the Ambient Water Mass

[38] Below the first few hundred meters, the characteristic water mass of the Amundsen Sea is upper CDW [*Jacobs et al.*, 1996]. Direct observations of this water mass on the Amundsen Sea continental shelf are too sparse to determine whether its properties have changed over recent decades. Geographically, the closest available data set is from the Ross Sea. *Jacobs et al.* [2002] analyzed this data set and indicate that CDW at 200 to 400 m depth in the coastal regions of this area has warmed by ~0.3°C over the period 1960 to 2000. They also report a freshening in both surface and deeper waters of 0.1–0.3 over the same period. Here we use these figures as a rough guide to the size of perturbation to apply to the properties of our ambient water mass. The standard experiment was repeated with anomalies in the range 0.0 to 0.5 applied to the ambient temperature (warming) and salinity (freshening) below 600 m water depth and with the gradient of temperature/salinity change from the surface to 600 m in equations (9) adjusted accordingly.

[39] Figure 14 shows the effect of temperature and salinity anomalies on the mean melt rate predicted by the model for PIIS proper. The mean melt rates in the standard experiment are 27.5 m yr^{-1} for PIIS proper and 20.6 m yr^{-1} for the whole ice shelf. The slight kinks in the contour lines are believed be due to averaging of the time dependence noted in section 4. The imposed freshening of 0.5 results in a minor <1 m yr^{-1} increase in melt rate; however, melt rates increase by up to ~8 m yr^{-1} in response to the 0.5°C warming. The spatial pattern of melt rate in these experiments showed only minor differences in comparison to the standard. While the effect of the warming is easily understood, the effect of freshening is more complex. A fresher plume favors reduced melt because the heat flux from the plume to the ice is moderated by the salt flux across the boundary layer [*Holland and Jenkins*, 1999]. However, the freshening was only applied to ambient water below 600 m depth, so that the strength of the stratification above that depth was reduced. The plume therefore loses buoyancy through entrainment at a lower rate and consequently maintains a higher speed. This in turn allows for higher heat and salt fluxes across the boundary layer and hence higher melt rates.

8. Discussion

[40] The spatial distribution of melt in both our tuned plume model and our estimates based on ice flux divergence suggest a highly localized pattern with maximum rates >100 m yr^{-1} within 20 km of the grounding line and relatively low rates (~10 m yr^{-1}) elsewhere. We chose to tune our model based on a mean melt rate of 26.2 m yr^{-1} for PIIS proper obtained from the ice flux divergence calculation. The sensitivity of the plume model to poorly constrained parameters suggests that we could equally well tune it to one of the other published estimates for melt rate. However, our chosen tuning does result in values for three of the four tuned parameters that are very close to their expected values. The exception is the core temperature of the ice shelf, the tuned value for which is ~10°C warmer than anticipated. The model's lack of sensitivity to ice

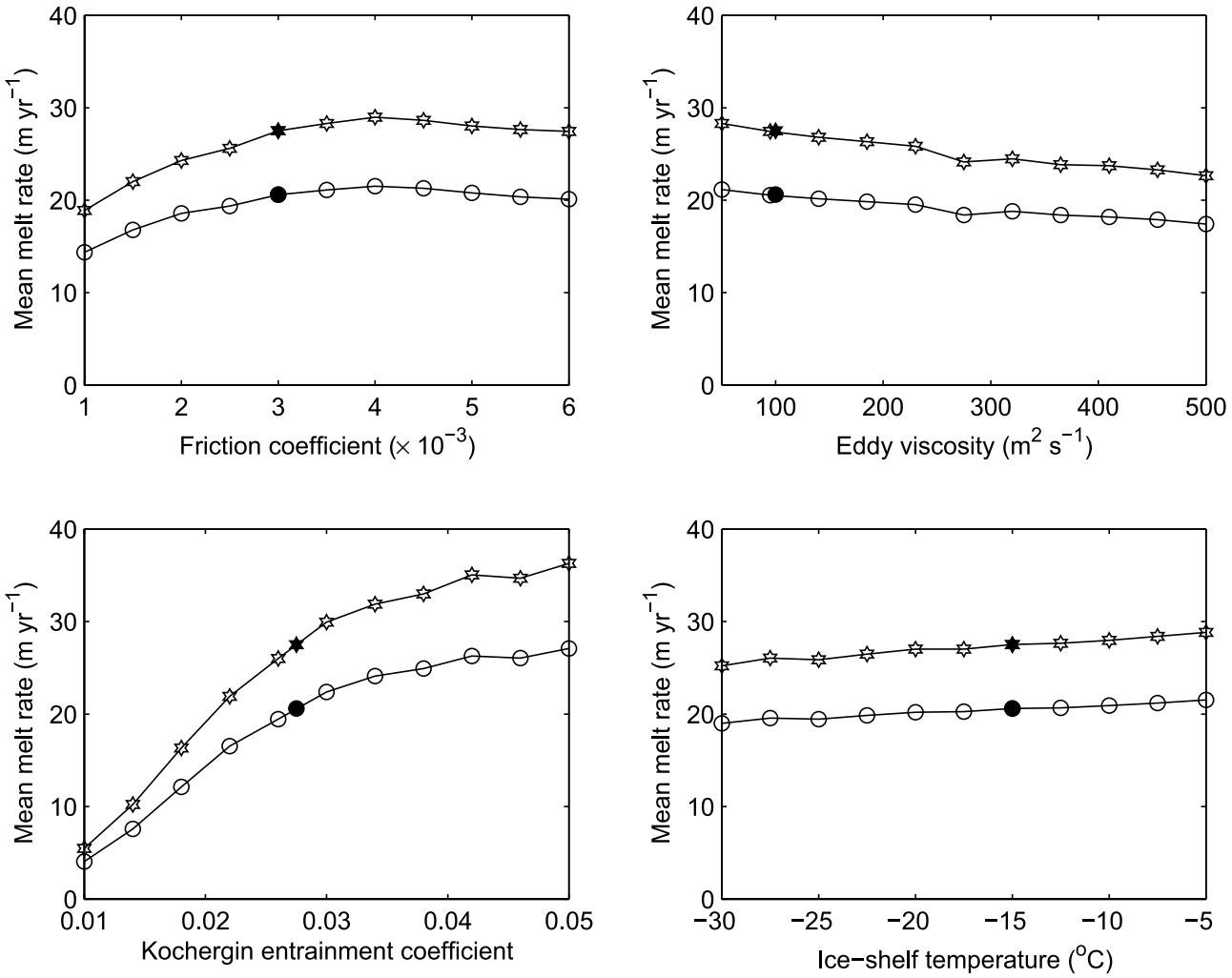

Figure 13. (top left) Effect of varying friction coefficient of the shelf underside, (top right) horizontal eddy viscosity, (bottom left) Kochergin entrainment coefficient, and (bottom right) bulk ice shelf temperature on the predicted mean melt rates (m yr^{-1}) for the whole ice shelf (circles) and for PIIS proper (stars). Standard values for these quantities are 0.003, 100 m^2 s^{-1}, 0.0275, and −15°C, respectively (indicated by solid symbols).

temperature (Figure 13) suggests that a more appropriate value could be employed without overly affecting our results. It is, however, possible that we have overestimated mean melt rate and that a lower estimate is more reasonable. A possible reason for this is that the estimate is dominated by high melt rates close to the grounding line, an area for which we do not have ice velocity measurements to tightly constrain the melt rate calculation. This mean melt rate is higher than previously published estimates; however, it does agree reasonably with other estimates based on ice flux divergence [*Rignot*, 1998]. Although the rate is approximately double that estimated from oceanographic data [*Jacobs et al.*, 1996], we suggest that considerable uncertainty enters the latter estimate in the determination of both the plume transport by assuming geostrophic balance and the properties of the inflowing and outflowing water masses. We note that the oceanographic data are not inconsistent with higher estimates of mean melt rate. While the mean melt rate predicted by our model is primarily a function of the poorly constrained entrainment coefficient and is therefore highly sensitive to tuning, the basic spatial pattern predicted by the model and summarized in section 4 is extremely robust and independent of any tuning.

[41] The model suggests that the path of the plume is largely controlled by the topography of the ice shelf underside and that its flow is geostrophic. Plume water outflow from PIIS proper is constrained to two inverted channels in the underside of the ice shelf. The more southerly channel lies under a shear margin within the ice shelf, created by fast flowing ice from PIG, while the northerly channel sits roughly in the center of the ice shelf and appears to be have been generated by a bedrock rise at PIG's ground line. This observation suggests that there may be potential for the interaction between plume and ice shelf dynamics; modeling suggests that the existence of a channel in the ice shelf underside enhances melt within the channel, which would deepen the feature further. The concentration

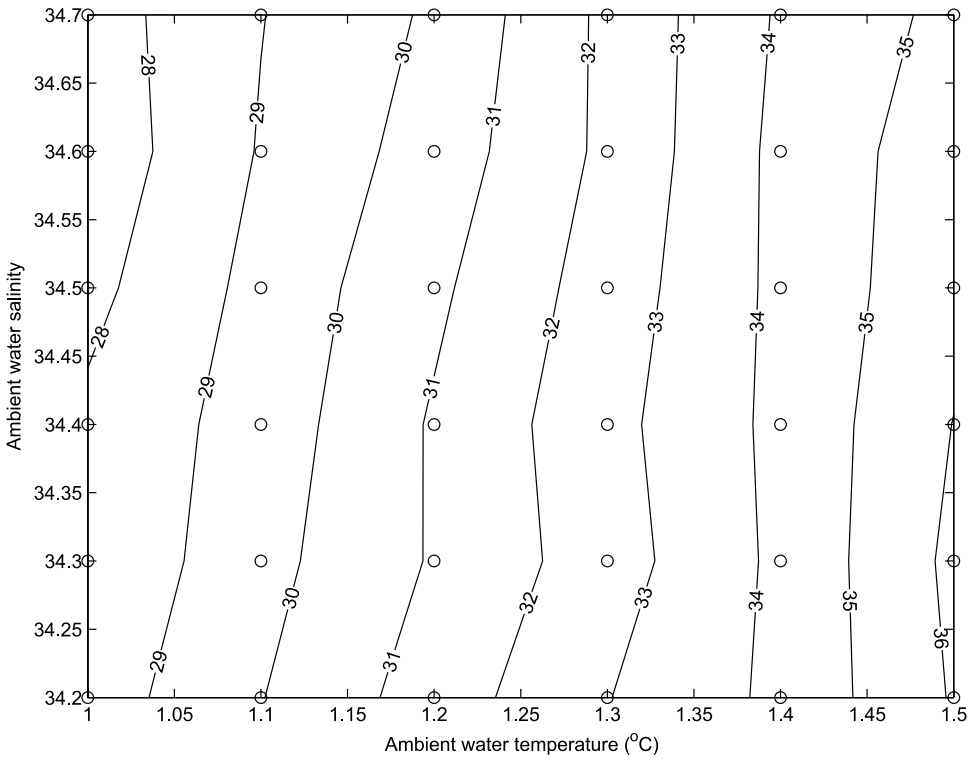

Figure 14. Effect of anomalies in ambient water temperature and salinity on predicted spatially averaged melt rates for PIIS proper (m yr^{-1}). The anomalies are applied to water at and below 600 m depth, and the parameters in equations (8) for water above 600 m are adjusted accordingly. Standard values are 1.0°C and 34.7. Open circles show locations of the model experiments in parameter space, on which the contours are based.

of plume flow within sub–ice shelf channels is a potential explanation for polynyas observed at the ice front of PIIS.

[42] The primary control on the simulated distribution of melt appears to be the topography of the ice shelf, in particular the very steep slopes within ~20 km of the grounding line. These slopes lead to high velocities (0.25–0.50 m s^{-1}) and high rates of entrainment. The majority of heat gained by the plume through the entrainment of warmer ambient waters is used in local melting within ~10 km of the site of entrainment. There is a nonlinear relationship between the temperature of the plume and the amount of melt generated: Rates of melt >100 m yr^{-1} are prevalent when plume water is >2°C above the interface freezing point; however, water at ~1.25°C above interface freezing point only generates melt rates ~10 m yr^{-1}. The simulations suggest that this effect arises because of the crucial role that plume velocity has in governing the amount of heat that can be used for melting, via its effect on heat diffusion through the boundary layer separating the plume and the ice shelf underside.

[43] Our modeling results suggest that a strong positive feedback may exist at the grounding line of PIG. The slope of the ice shelf underside in this area is responsible for the generation of locally very high melt rates because of its role in producing high plume velocities and high rates of entrainment. We speculate that increases in subshelf melt rate will increase these slopes, so that a further increase in melt rate is to be expected. This positive feedback would be potentially unstable if the ice shelf were not flowing because of ice deformation; however, the steepened ice shelf underside will generate steeper upper ice surface topography (through simple hydrostatic balance) and an increase in the gravitational driving stresses forcing ice deformation. The consequent increase in ice flow could then act to reduce ice thickness gradients and counteract the initial steepening. There is therefore potential for a delicate interaction between ice flow, ice shelf geometry, and melt close to the grounding line. A coupled ice shelf flow and plume circulation model would be required to explore this interaction.

[44] We assessed the response of the plume model to changes in ambient water temperature and obtained a linear sensitivity of mean melt rate under PIIS proper to small positive perturbations of CDW temperature of ~16 m yr^{-1} $°C^{-1}$. We do not contend that this is true for larger changes in temperature (particularly negative changes) or other ice shelf topographies. This figure is slightly higher than the 12 m yr^{-1} $°C^{-1}$ found for similar temperature perturbations by *Hellmer et al.* [1998] from modeling of the circulation beneath PIIS. Some care is required in comparing this sensitivity to the observed rates of ice shelf thinning along the coast of the Amundsen Sea for two reasons. First, the observed thinning rates are not simply a reflection of the melt rate perturbation but include the response of the ice shelf flow to any alterations in its geometry. This effect is likely to ensure that the observed thinning rate is less than the increase in melt rate that generated it because a generally thinner ice shelf is likely to spread more slowly and to

thicken in response to the initial thinning. Second, in conducting our analysis we assumed that the perturbations were applied instantaneously. This is very unlikely to have happened in reality; indeed, the best available time series of temperature in the area (from the nearby Ross Sea [*Jacobs et al.*, 2002]) supports a warming of ~0.3°C over a period of 40 years. Given these caveats, our estimate of the sensitivity of PIIS's melt to CDW temperature change suggests that the thinning that PIIS experienced during the period 1992 to 2001 (at rate of 3.9 ± 0.5 m yr^{-1} [*Shepherd et al.*, 2002]) would require a hypothetical warming of at least ~0.25°C in the CDW beneath PIIS.

[45] **Acknowledgments.** This work was supported by the UK Natural Environment Research Council's funding of the Centre for Polar Observation and Modelling. We would like to acknowledge that the image shown in Figure 11 was obtained from the NASA/GSFC/METI/ERSDAC/JAROS and U.S./Japan ASTER Science Team. Finally, we would like to thank Stan Jacobs (who commented on an early draft of the paper) and three anonymous reviewers for their useful suggestions.

References

Bamber, J. L., and R. A. Bindschadler (1997), An improved elevation dataset for climate and ice-sheet modeling: Validation with satellite imagery, *Ann. Glaciol.*, *25*, 438–444.

Corr, H. F. J., C. S. M. Doake, A. Jenkins, and D. G. Vaughan (2001), Investigations of an "ice plain" in the mouth of Pine Island Glacier, Antarctica, *J. Glaciol.*, *47*(156), 51–57.

Gade, H. G. (1979), Melting of ice in sea water; a primitive model with application to the Antarctic ice shelf and icebergs, *J. Phys. Oceanogr.*, *9*(1), 189–198.

Gerdes, R., J. Determann, and K. Grosfeld (1999), Ocean circulation beneath Filchner-Ronne Ice Shelf from three-dimensional model results, *J. Geophys. Res.*, *104*(C7), 15,827–15,842.

Giovinetto, M. B., N. M. Waters, and C. R. Bentley (1990), Dependence of Antarctic surface mass balance on temperature, elevation, and distance to open ocean, *J. Geophys. Res.*, *95*(D4), 3517–3531.

Grosfeld, K., R. Gerdes, and J. Determann (1997), Thermohaline circulation and interaction between ice shelf cavities and the adjacent open ocean, *J. Geophys. Res.*, *102*(C7), 15,595–15,610.

Hellmer, H. H., S. S. Jacobs, and A. Jenkins (1998), Oceanic erosion of a floating Antarctic glacier in the Amundsen Sea, in *Ocean, Ice, and Atmosphere: Interactions at the Antarctic Continental Margin*, edited by S. Jacobs and R. Weiss, pp. 83–99, AGU, Washington D. C.

Holland, D. M., and A. Jenkins (1999), Modeling thermodynamic ice-ocean interactions at the base of an ice shelf, *J. Phys. Oceanogr.*, *29*(8), 1787–1800.

Holland, D. M., S. S. Jacobs, and A. Jenkins (2003), Modelling the ocean circulation beneath the Ross Ice Shelf, *Antarct. Sci.*, *15*(1), 13–23.

Holland, P. R., and D. L. Feltham (2006), The effects of rotation and ice shelf topography on frazil-laden Ice Shelf Water plumes, *J. Phys. Oceanogr.*, *36*(12), 2312–2327.

Jacobs, S. S., H. H. Hellmer, and A. Jenkins (1996), Antarctic ice sheet melting in the Southeast Pacific, *Geophys. Res. Lett.*, *23*(9), 957–960.

Jacobs, S. S., C. F. Giulivi, and P. A. Mele (2002), Freshening of the Ross Sea during the late 20th century, *Science*, *297*(5580), 386–389.

Jenkins, A. (1991), A one-dimensional model of ice shelf-ocean interaction, *J. Geophys. Res.*, *96*(C11), 20,671–20,677.

Jenkins, A. (1999), Impact of melting ice on ocean waters, *J. Phys. Oceanogr.*, *29*(9), 2370–2381.

Jenkins, A., and A. Bombosch (1995), Modeling the effects of frazil ice crystals on the dynamics and thermodynamics of Ice Shelf Water plumes, *J. Geophys. Res.*, *100*(C4), 6967–6981.

Jenkins, A., D. G. Vaughan, S. S. Jacobs, H. H. Hellmer, and J. R. Keys (1997), Glaciological and oceanographic evidence of high melt rates beneath Pine Island Glacier, West Antarctica, *J. Glaciol.*, *43*(143), 114–121.

Jenkins, A., H. H. Hellmer, and D. M. Holland (2001), The role of meltwater advection in the formulation of conservative boundary conditions at an ice-ocean interface, *J. Phys. Oceanogr.*, *31*(1), 285–296.

Jenkins, A., D. M. Holland, K. W. Nicholls, M. Schröder, and S. Østerhus (2004), Seasonal ventilation of the cavity beneath Filchner-Ronne Ice Shelf simulated with an isopycnic coordinate ocean model, *J. Geophys. Res.*, *109*, C01024, doi:10.1029/2001JC001086.

Joughin, I., E. Rignot, C. E. Rosanova, B. K. Lucchitta, and J. Bohlander (2003), Timing of recent accelerations of Pine Island Glacier, Antarctica, *Geophys. Res. Lett.*, *30*(13), 1706, doi:10.1029/2003GL017609.

Jungclaus, J. H., and J. O. Backhaus (1994), Application of a transient reduced gravity plume model to the Denmark Strait Overflow, *J. Geophys. Res.*, *99*(C6), 12,375–12,396.

Jungclaus, J. H., J. O. Backhaus, and H. Fohrmann (1995), Outflow of dense water from the Storfjord in Svalbard: A numerical model study, *J. Geophys. Res.*, *100*(C12), 24,719–24,728.

Kader, B. A., and A. M. Yaglom (1977), Turbulent heat and mass transfer from a wall with parallel roughness ridges, *Int. J. Heat Mass Transfer*, *20*, 345–357.

Kochergin, V. P. (1987), Three-dimensional prognostic models, in *Three-dimensional coastal ocean models*, edited by N. S. Heaps, pp. 201–208, AGU, Washington, D. C.

Lowe, A. L., and J. B. Anderson (2002), Reconstruction of the West Antarctic ice sheet in Pine Island Bay during the Last Glacial Maximum and its subsequent retreat history, *Quat. Sci. Rev.*, *21*, 1879–1897.

Mellor, G. L., and P. A. Durbin (1975), The structure and dynamics of the ocean surface mixed layer., *J. Phys. Oceanogr.*, *5*(4), 718–728.

Mesinger, F., and A. Arakawa (1976), *Numerical Methods Used in Atmospheric Models*, *GARP Publ. Ser.*, vol. 1, 63 pp., World Meteorol. Org., Geneva.

Nicholls, K. W., and A. Jenkins (1993), Temperature and salinity beneath Ronne Ice Shelf, Antarctica, *J. Geophys. Res.*, *98*(C12), 22,553–22,568.

Payne, A. J., A. Vieli, A. P. Shepherd, D. J. Wingham, and E. Rignot (2004), Recent dramatic thinning of largest West Antarctic ice stream triggered by oceans, *Geophys. Res. Lett.*, *31*, L23401, doi:10.1029/2004GL021284.

Rignot, E. J. (1998), Fast recession of a West Antarctic glacier, *Science*, *281*(5376), 549–551.

Rignot, E. (2002), Ice shelf changes in Pine Island Bay, Antarctica, 1947–2000, *J. Glaciol.*, *48*(161), 247–256.

Rignot, E., D. G. Vaughan, M. Schmeltz, T. Dupont, and D. MacAyeal (2002), Acceleration of Pine Island and Thwaites glaciers, West Antarctica, *Ann. Glaciol.*, *34*, 189–194.

Schmeltz, M., E. Rignot, T. K. Dupont, and D. R. MacAyeal (2002), Sensitivity of Pine Island Glacier, West Antarctica, to changes in ice shelf and basal conditions: A model study, *J. Glaciol.*, *48*(163), 552–558.

Shepherd, A., D. J. Wingham, and J. A. D. Mansley (2002), Inland thinning of the Amundsen Sea sector, West Antarctica, *Geophys. Res. Lett.*, *29*(10), 1364, doi:10.1029/2001GL014183.

Shepherd, A., D. Wingham, and E. Rignot (2004), Warm ocean is eroding West Antarctic Ice Sheet, *Geophys. Res. Lett.*, *31*, L23402, doi:10.1029/2004GL021106.

Williams, M. J. M., K. Grosfeld, R. C. Warner, R. Gerdes, and J. Determann (2001), Ocean circulation and ice-ocean interaction beneath the Amery Ice Shelf, Antarctica, *J. Geophys. Res.*, *106*(C10), 22,383–22,399.

P. R. Holland and A. Jenkins, British Antarctic Survey, High Cross, Madingley Road, Cambridge CB3 0ET, UK.

I. Joughin, Polar Science Center, Applied Physics Laboratory, University of Washington, 1013 NE 40th Street, Seattle, WA 98105-6698, USA.

A. J. Payne and I. C. Rutt, CPOM, University of Bristol, University Road, Bristol BS8 1SS, UK. (a.j.payne@bristol.ac.uk)

A. P. Shepherd, CPOM, Scott Polar Research Institute, University of Cambridge, Cambridge CB2 1ER, UK.